Nano Energy 73 (2020) 104838

Contents lists available at ScienceDirect

Nano Energy

journal homepage: http://www.elsevier.com/locate/nanoen

Intercalation pseudocapacitance of $FeVO_4{\cdot}nH_2O$ nanowires anode for high-energy and high-power sodium-ion capacitor

Jun Dong [a,1], Yi He [a,1], Yalong Jiang [a], Shuangshuang Tan [a], Qiulong Wei [b,*], Fangyu Xiong [a], Zhaolong Chu [a], Qinyou An [a], Liqiang Mai [a,c,*]

[a] State Key Laboratory of Advanced Technology for Materials Synthesis and Processing, Wuhan University of Technology, Wuhan 430070, China
[b] Department of Materials Science and Engineering, Fujian Key Laboratory of Materials Genome, College of Materials, Xiamen University, Xiamen, 361005, China
[c] Foshan Xianhu Laboratory of the Advanced Energy Science and Technology Guangdong Laboratory, Xianhu hydrogen Valley, Foshan 528200, China

ARTICLE INFO

Keywords:
Sodium-ion capacitors
Intercalation pseudocapacitance
Hybrid supercapacitors
$FeVO_4{\cdot}nH_2O$ nanowires
Sodium-ion storage

ABSTRACT

Sodium-ion capacitors (SICs) can effectively deliver both high energy and power density, which are appropriate for high-rate demanding applications at low-cost. At present, the most developed SICs utilize electric double-layer capacitance (EDLC)-type cathode and battery-type anode, but their capacity is very limited and assembly technique is complex with an inevitable pre-sodiation process. Herein, through systematically comparing the lithium-ion and sodium-ion storage behaviors of $FeVO_4{\cdot}0.6H_2O$ nanowires anode, the sodium-ion intercalation mechanism is deeply understood. The $FeVO_4{\cdot}0.6H_2O$ anode presents pseudocapacitive sodium-ion intercalation behavior, over 93% of total capacity from capacitive contribution, identified by kinetics analysis, operando XRD and *ex-situ* TEM characterizations. The $FeVO_4{\cdot}0.6H_2O$ anode displays high specific capacity, high initial coulombic efficiency, remarkable rate capability and cycling stability for sodium-ion intercalation. Benefiting from the high-performance pseudocapacitive $FeVO_4{\cdot}0.6H_2O$ anode, it is coupled with Na-rich high-rate battery-type cathode ($Na_3(VO)_2(PO_4)_2F$/rGO) to construct a novel non-aqueous SIC without any additional pre-sodiation process. The assembled SIC delivers a maximum energy density up to 88 Wh kg^{-1} (at 95 W kg^{-1}) and a high power density of 7.9 kW kg^{-1} (with 35 Wh kg^{-1}), and superior cycling stability (5000 cycles). The anode and cathode operate under very safe potential range, respectively, enabling the high safety of SIC even at rapid rates. Our work presents the significant advantages of pseudocapacitive sodium-ion intercalation anode for obtaining both high energy and high power sodium storage devices.

1. Introduction

Rechargeable sodium-ion storage devices, including sodium-ion batteries (SIBs) and capacitors (SICs), are considered as one of the most promising alternatives to those of lithium-ion counterparts for large-scale applications [1–4]. The low-cost sodium-based chemicals reduce the price of SIBs and SICs [5]. More importantly, the much abundant resources of sodium than those of lithium (23,000 *vs.* 17 ppm in earth's crust) could make the promising widespread usages of SIBs and SICs [6–8].

The Nobel Prize in Chemistry 2019 is awarded to J.B. Goodenough, M.S. Whittingham and A. Yoshino for their contributions to the development of lithium-ion battery (LIB) [9]. Historically, the concept of electrochemical lithium-ion intercalation was firstly discovered in the 1970's by Whittingham and co-workers [10–14]. Following the lithium-ion intercalation chemistry, sodium-ion intercalation has been demonstrated as well [15–19]. However, sodium-ion intercalation shows very different phase change behavior (*e.g.* coordination, lattice constant, crystal structure) and diffusion properties when compared to those of lithium-ion, owing to the larger ionic radius of Na^+ (1.02 Å *vs.* 0.76 Å for Li^+) [1]. The reduction potential of −2.71 V (*vs.* SHE) for Na^+ is higher than that of −3.04 V (*vs.* SHE) for Li^+ [20,21]. Generally, the storage capacity, operating voltage and energy density of SIBs/SICs are lower than those of lithium-ion counterparts [22]. But, it is worth noting that the larger Na^+ present a lower activation energy of ionic diffusion and smaller Stokes' radius in solvent, resulting in higher mobility of $[Na\text{-solvent}]^+$ and ionic conductivity than that of Li^+ system [20,21]. Hence, it is proposed that the high-power SICs are very promising for

* Corresponding authors.
E-mail addresses: qlwei@xmu.edu.cn (Q. Wei), mlq518@whut.edu.cn (L. Mai).
[1] These authors contribute equally to this work.

https://doi.org/10.1016/j.nanoen.2020.104838
Received 6 March 2020; Received in revised form 5 April 2020; Accepted 10 April 2020
Available online 18 April 2020

replacing the present lithium-ion capacitors (LICs), since the rational use of low-cost sodium resources for large-scale applications. However, there are still some challenges for the development of SICs, including the design of high-rate sodium-ion storage electrode materials and their rapid charge-discharge mechanism [2,23].

Pseudocapacitive materials store charge through battery-like Faradaic redox reactions but display rapid rates comparable to those of electric double-layer capacitors [24]. Dunn and co-workers summarized the various transition metal oxides (TMOs) exhibiting pseudocapacitive behaviors [24]. Notably, the pseudocapacitive lithium-ion intercalation anode materials, such as *T*-Nb_2O_5 [25], TiO_2(B) [26], MoS_2 [16] and MoO_3 [27], deliver ultrahigh-rate performance and are suitable for the development of high-energy and high-power hybrid LICs. Recently, Nb_2O_5 and TiO_2 anode with pseudocapacitive behavior were also investigated for Na^+ storage [28,29]. However, their low initial coulombic efficiency results in an irreversible consumption of electrolyte, which is still unsatisfied [24]. It is assumed that developing the pseudocapacitive sodium-ion intercalation materials is promising approach for high-rate Na^+ storage and high-performance SICs. However, it is rarely reported and remains largely unexplored.

The Faradaic reaction is highly depended on the redox of transition metals. Ferric vanadate is an attracting electrode owing to both Fe^{3+} and V^{5+} exhibiting electrochemical redox activity, resulting in multi-electron reactions and high capacity [30–35]. $FeVO_4{\cdot}nH_2O$ nanowires for Li^+ storage deliver a specific capacity of 1300 mAh g^{-1} in the potential range of 0.02–3.5 V (*vs.* Li^+/Li), corresponding to about 9 Li^+ ions per unit formula [31]. However, the Na^+ storage mechanism and electrochemical behavior of $FeVO_4{\cdot}nH_2O$ have not been investigated yet. A deep understanding of the difference between the electrochemical reaction of Li^+ and Na^+ storage would help the design of high-performance energy storage devices. Herein, we systematically investigate the Na^+ and Li^+ storage behaviors of $FeVO_4{\cdot}nH_2O$ by electrochemical test, operando X-ray diffraction (XRD) and *ex-situ* TEM. It is found that the Na^+ and Li^+ intercalation reaction presents a pseudocapacitive behavior, which contributes to high initial coulombic efficiency (ICE), reversible cycling and high-rate capability. Based on the highly pseudocapacitive $FeVO_4{\cdot}nH_2O$ anode, we assemble a SIC without any additional pre-sodiation processes. The electrochemical behaviors of the SIC are intensively studied by three-electrode and two-electrode systems. The SIC delivers expected a maximum energy density up to 88 Wh kg^{-1} (at the power density of 95 W kg^{-1}) and a high power density of 7.9 kW kg^{-1}(with the energy density of 35 Wh kg^{-1}), and superior cycling stability (5000 cycles).

2. Experimental section

2.1. Experimental methods

2.1.1. Synthesis of $FeVO_4{\cdot}nH_2O$ nanowires

The $FeVO_4{\cdot}nH_2O$ nanowires were prepared by a facile hydrothermal method [36,37]. Briefly, 4 mmol $FeCl_3{\cdot}6H_2O$ was dissolved in 20 mL deionized water under stirring. 4 mmol NH_4VO_3 was dissolved in another 20 mL deionized water at 80 °C. Then, the NH_4VO_3 solution was slowly added into the $FeCl_3{\cdot}6H_2O$ solution under stirring to form a suspension. After 10 min, the suspension was transferred into a 50 mL Teflon-lined stainless steel autoclave and heated at 180 °C for 4 h. The final precipitate was washed by centrifugation with deionized water and ethanol for each three times. Finally, the $FeVO_4{\cdot}nH_2O$ nanowires powders were obtained after drying under vacuum at 70 °C for 12 h.

2.1.2. Synthesis of $Na_3(VO)_2(PO_4)_2F$/rGO composites

The $Na_3(VO)_2(PO_4)_2F$/rGO (NVOPF/rGO) was synthesized by one-pot solvothermal method. Graphene oxide (GO) was prepared by the Hummers' method [38]. Firstly, 2 mmol NH_4VO_3, 3 mmol NaF and 2 mmol $NH_4H_2PO_4$ were dissolved in 20 mL GO dispersion (2 g L^{-1}) under stirring. Then, 20 mL N,N-dimethylform amide (DMF) was slowly added to the above mixture with stirring for 1 h. The resulting solution was transferred into a 50 mL Teflon-lined stainless steel autoclave and heated at 180 °C for 24 h. Finally, the final precipitate was washed by deionized water and ethanol for three times, and then NVOPF/rGO powders were obtained after drying in a vacuum oven at 100 °C for 12 h.

2.2. Materials characterization

X-ray diffraction (XRD) measurements were conducted by using a D8 Advance X-ray diffractometer with a non-monochromated Cu Kα X-ray source at room temperature. Scanning electron microscopy (SEM) images were collected using a JEOL-7100F microscope. Transmission electron microscopy and high-resolution TEM (HRTEM) images were collected by using a JEM-2100F STEM/EDS microscope. Thermogravimetric (TG) analysis was performed using NETZSCH-STA449F5 thermoanalyzer. The carbon content analyses were performed with CHNS elemental analyzer.

2.3. Electrochemical measurements

The coin cells (CR2016) and three-electrode device and operando cells were assembled in an Ar-filled glove box. The working electrode of $FeVO_4{\cdot}0.6H_2O$ was prepared by mixing 80% active materials, 12% conductive carbon and 8% carboxyl methyl cellulose (CMC). Then, the slurries were coated onto the carbon coated Al foil or Cu foil for Na^+ or Li^+ storage test, respectively. The NVOPF/rGO electrode was made by mixing 70% active materials, 20% conductive carbon and 10% polyvinylidene fluoridein (PVDF). Then, the homogeneous slurries were coated onto the carbon coated Al foil and dried in a vacuum oven at 70 °C for 12 h. The mass loading of $FeVO_4{\cdot}0.6H_2O$ and NVOPF/rGO was ~1 and ~2 mg cm^{-2}, respectively. To assemble the sodium-ion coin cell, the working electrode was a disk with a diameter of 10 mm; sodium disk (a diameter of 14 mm) was used as the counter and reference electrode; Celgard-2350 film was used as separator, and 1 M $NaPF_6$ in diethylene glycol dimethyl ether was used as the electrolyte. To assemble the three-electrode device, the assembling diagram was presented in Fig. 4a, in which sodium ring (inner diameter of 17 mm, outer diameter of 24 mm) was used as the reference electrode. To assemble lithium-ion coin cell, lithium disk (a diameter of 14 mm) was used as the counter and reference electrode; Celgard-2400 separator was used; 1 M lithium hexafluorophosphate ($LiPF_6$) solution in ethylene carbon–dimethyl carbonate (1:1 vol/vol) was used as electrolyte. Galvanostatic charge-discharge rate performance and cyclic voltammetry were performed by using Bio-Logic VMP3 potentiostat at room temperature. The long-term cycling performance was performed by using NEWARE battery testing system.

3. Results and discussion

3.1. Characterizations of $FeVO_4{\cdot}nH_2O$ nanowires

The $FeVO_4{\cdot}nH_2O$ nanowires powder is in yellow (inset of Fig. S1a) [36]. The powder XRD of the product is shown in Fig. S1a. All the diffractions are indexed to Fervanite ($FeVO_4{\cdot}nH_2O$, JCPDS card No. 27–0257) [34,36]. Fourier transform infrared (FTIR) spectrum further characterizes the Fe–O, V–O, V–O–Fe and V–O–Fe stretching modes and demonstrates the existence of crystal water (Fig. S1b). The number of water molecules in $FeVO_4{\cdot}nH_2O$ is 0.6, depicted by thermal gravity analysis (Fig. S1c). The chemical formula of the obtained product is $FeVO_4{\cdot}0.6H_2O$. The scanning electron microscope (SEM) image (Fig. S1d) displays nanowire morphology of $FeVO_4{\cdot}0.6H_2O$. Transmission electron microscopy (TEM) image (Fig. S1e) shows the nanowire with a width of about 100 nm and a length of several micrometers. Fig. S1f shows the high-resolution TEM (HRTEM) image of $FeVO_4{\cdot}0.6H_2O$ nanowire. The measured 8.1 Å inter distance is in agreement with (100) plane of $FeVO_4{\cdot}0.6H_2O$ lattice [32].

3.2. Lithium-ion and sodium-ion storage mechanism

The electrochemical performance and storage mechanism of $FeVO_4{\cdot}0.6H_2O$ were investigated by assembling half cell (2016-type and operando XRD measurement cell), in which the lithium or sodium foil was used as the counter and reference electrode. At first, we investigated the lithium-ion intercalation behavior, then parallelly compared to that of sodium-ion intercalation. Fig. 1a shows the cyclic voltammetry (CV) curves in the potential range of 1–3 V *vs.* Li^+/Li. The CV curves show a broad cathodic peak at ~2.3 V and a sharp cathodic peak at ~1.6 V. All the peaks disappeared at the following de-lithiation process and 2nd repeated cycle. The galvanostatic (GV) discharge-charge profiles at 0.1 A g^{-1} (Fig. 1b) shows the same result to CV curves. The lithiation process from an initial state to 2 V displays a linear-like capacitive slop curve, corresponding to the intercalation numbers of 1.3 Li^+ ions per formula unit. Then continuous discharging, an obvious plateau at ~1.6 V *vs.* Li^+/Li was observed. The lithiation numbers are 3.4 Li^+ ions per formula when discharged to 1 V. When it is charged to 3 V, the de-lithiation process is quite different, indicating an irreversible process. The reversible Li^+ storage number of $FeVO_4{\cdot}0.6H_2O$ anode is 2.2 Li^+ ions per formula unit. Operando XRD patterns were used to investigate the Li^+ storage mechanism, as shown in Fig. 1c. The diffraction peaks at 27.7°, 30.4° and 34.2° are indexed to $FeVO_4{\cdot}0.6H_2O$. The first lithiation process can be separated into three steps. The corresponding schematic is displayed in Fig. 1k. At the first step, the diffraction peaks continuously shift toward a lower angle, from 27.7° to 27.0°, 30.4° to 30.2° and 34.2° to 34.0°, respectively. This step is the lithium intercalation into the $FeVO_4{\cdot}0.6H_2O$ under a single-phase reaction. At the second step, it occurs at the plateau reaction of ~1.6 V, the intensity of diffraction peaks gradually weakens even to totally disappear, corresponding to an irreversible transformation from crystalline $FeVO_4{\cdot}0.6H_2O$ into amorphous state. The third step is continuous lithiation of amorphous sample, accompanied with no peaks observed in XRD patterns. During charging back to 3 V, all diffraction peaks remain disappearance. The linear-like charge profile is quite different from the initial discharge curve, corresponding to an irreversible process. The $FeVO_4{\cdot}0.6H_2O$ nanowires at the

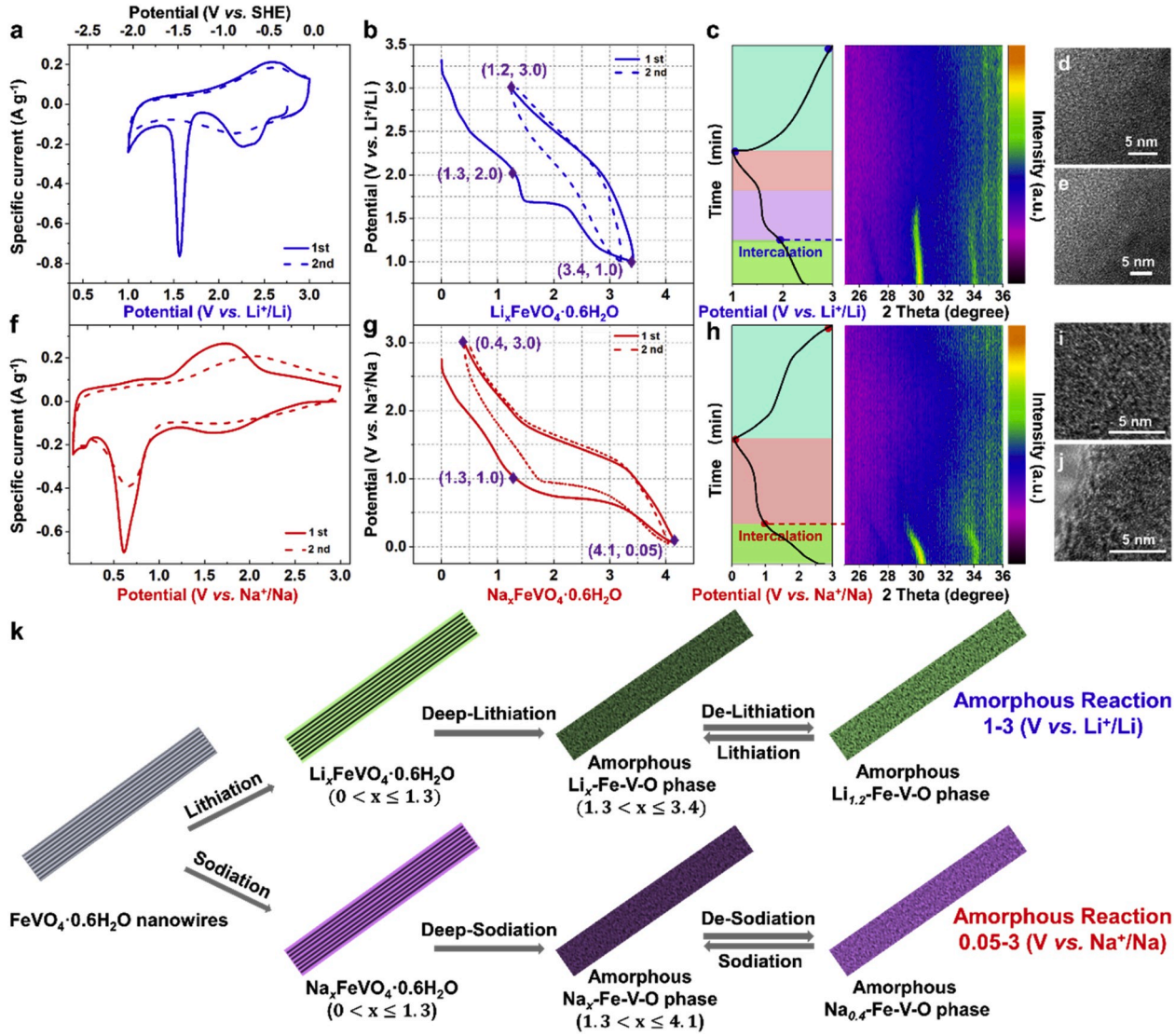

Fig. 1. Lithium-ion and sodium-ion storage mechanism of $FeVO_4{\cdot}0.6H_2O$. For Li^+ storage in 1–3 V *vs.* Li^+/Li, CV curves (a) and potential *vs.* composition profiles (b) of $FeVO_4{\cdot}0.6H_2O$ nanowires, respectively; (c) operando XRD pattern during galvanostatic test at 0.1 A g^{-1}; (d, e) *ex-situ* HRTEM images of $FeVO_4{\cdot}0.6H_2O$ nanowires when discharged to 1 V *vs.* Li^+/Li and charged to 3 V *vs.* Li^+/Li, respectively. For Na^+ storage in 0.05–3 V *vs.* Na^+/Na, CV curves (f) and potential *vs.* composition profiles (g) of $FeVO_4{\cdot}0.6H_2O$ nanowires, respectively; (h) operando XRD pattern during galvanostatic test at 0.1 A g^{-1}; (i, j) *ex-situ* HRTEM images of $FeVO_4{\cdot}0.6H_2O$ nanowires when discharged to 0.05 V *vs.* Na^+/Na and charged to 3 V *vs.* Na^+/Na, respectively. (k) A schematic diagram of the similarity and difference in $FeVO_4{\cdot}0.6H_2O$ for Li^+ and Na^+ storage mechanism after deep-lithiation/sodiation.

discharged state (Fig. S2a and Fig. 1d) and charged state (Fig. S2b and Fig. 1e) were characterized by TEM and HRTEM, respectively. The results show that the $FeVO_4{\cdot}0.6H_2O$ maintains the nanowires morphology but turns to amorphous state, which are consistent with the observation by operando XRD. Owing to the irreversible amorphous transformation occurred below 2 V *vs.* Li^+/Li, a potential range of 2–3 V *vs.* Li^+/Li is selected to investigate the Li^+ intercalation behaviors of $FeVO_4{\cdot}0.6H_2O$ (Fig. S3), which delivers much reversible storage of 1.12 Li^+ ions per formula unit and a high ICE of 89%.

Subsequently, the electrochemical Na^+ storage behavior and mechanism were investigated systematically. Fig. 1f shows the CV curves in the potential range of 0.05–3 V *vs.* Na^+/Na. There are broad cathodic peak at ~1.65 V and sharp cathodic peak at ~0.6 V, and broad anodic peak at ~1.7 V in the 1st cycle. Then, the cathodic peak current decreases in the next cycle, indicating an irreversible redox process. The GV charge-discharge profiles when initial discharged to 1 V displays a linear slop curve, which is a typical capacitive behavior, as shown in Fig. 1g. The intercalation numbers are 1.3 Na^+ ions per formula unit. Then continuous discharging to 0.05 V, an obvious plateau at ~0.6 V *vs.* Na^+/Na is observed and the related amount of Na^+ storage corresponds to 4.1 Na^+ ions per formula unit. When charged to 3 V, the de-sodiation plateau is at ~1.7 V. Approximately 3.7 Na^+ ions per formula unit are de-sodiated, thus the amount of irreversible Na^+ ions is ~0.4. The operando XRD patterns are collected as well to figure out the Na^+ storage mechanism of $FeVO_4{\cdot}0.6H_2O$ (Fig. 1h). Different from the lithiation process as discussed above, the initial sodiation process only includes two steps. From initial state to 1 V, the diffraction peaks continuously shift toward lower angle, from 27.7° to 26.6°, 30.4° to 29.3° and 34.2° to 33.6°, respectively, indicating a single-phase sodium-ion intercalation behavior. The lower angle shifts are related to the enlarging volume of crystal structure during sodium-ion intercalation. At the second step, the diffraction peaks almost disappear at the beginning of discharge potential at 1 V *vs.* Na^+/Na, corresponding to irreversible transformation from crystalline into amorphous state. The discharge plateau at ~0.6 V is the sodiation of amorphous Na_x-Fe-V-O phase. After charging back to 3 V, no diffraction peaks are recovered. Amorphous $FeVO_4{\cdot}0.6H_2O$ nanowires were observed by TEM (Figs. S2c and d) and HRTEM (Fig. 1i and j) images at the sodiated and desodiated states, respectively, which were consistent with the results of operando XRD.

Based on the above results, the detailed charge storage mechanism of $FeVO_4{\cdot}0.6H_2O$ for both Li^+ and Na^+ storage is schematically shown in Fig. 1k. $FeVO_4{\cdot}0.6H_2O$ electrode for the Li^+ and Na^+ storage undergoes similar reaction processes, including intercalation of Na^+ (or Li^+) into $FeVO_4{\cdot}0.6H_2O$ through single-phase reaction and the amorphous transformation of crystalline $FeVO_4{\cdot}0.6H_2O$ after deep reaction. However, there are some differences between the Li^+ and Na^+ storage processes. At the intercalation process, the intercalation amount of Li^+ and Na^+ ions are similar, but the XRD peaks of $FeVO_4{\cdot}0.6H_2O$ present a larger shift for Na^+ storage than those for Li^+ storage (Fig. 1c and h). This difference indicates slightly enlarged lattice expansion by Na^+ intercalation, which is possibly caused by a larger ionic radius of Na^+ than that of Li^+. Interestingly, the amorphous transformation step is also quite different between the Li^+ and Na^+ storage. The amorphous transformation for lithiation accompanies with a discharge plateau (namely conversion reaction [32,39]), while the operando XRD peaks gradually weaken during the plateau reaction and then totally disappear. However, the amorphous transformation caused by sodiation directly occurs after the sodium-ion intercalation step that is before the plateau reaction, which may be due to excessive volume expansion caused by the over number of Na^+ intercalation. The related cycling stabilities are extremely poor after irreversible amorphous transformation taking place (Figs. S4a and b). The capacity retention is only 20% for Li^+ storage and 18% for Na^+ storage after 100 cycles, respectively.

3.3. Pseudocapacitive sodium-ion intercalation behavior of $FeVO_4{\cdot}0.6H_2O$

Inhibiting the irreversible amorphous transformation is a key measure for optimizing the electrochemical performance [40,41]. According to above investigation, the potential window is set in the range of 1–3 V *vs.* Na^+/Na, while only sodium-ion intercalation process is involved. Fig. 2a shows the first and second CV curves in the potential range of 1–3 V *vs.* Na^+/Na, which only displays a pseudo-rectangular shape. Fig. 2b shows the potential *vs.* composition profiles of $FeVO_4{\cdot}0.6H_2O$ nanowires in 1–3 V *vs.* Na^+/Na. The charge-discharge curves display a capacitive-like voltage response, consistent with the result of CV test. The total amount of Na^+ storage is 1.3 per formula unit, and the amount of reversible Na^+ is 1.08, corresponding to an ICE of 83%. Besides, the operando XRD patterns are tested at the current density of 0.1 A g^{-1} in the potential range of 1–3 V (Fig. 2c). The diffraction peaks of $FeVO_4{\cdot}0.6H_2O$ shift towards lower angle (from 27.7° to 26.6°, 30.4° to 29.3° and 34.2° to 33.6°) and then returns to its original position during sodiation and de-sodiation processes, indicating the highly reversible (de)intercalation processes. The different (de)sodiated states of $FeVO_4{\cdot}0.6H_2O$ nanowires were characterized by TEM (Figs. S5a and b, respectively) and HRTEM (Fig. 2d and e, respectively), which showed the crystalline nanowire morphology. Compared to the HRTEM image of initial $FeVO_4{\cdot}0.6H_2O$ nanowires (Fig. S1f), the spacing of (100) plane at the discharged state of 1 V is slightly increased from 8.1 to 8.3 Å (Fig. 2d). Then, the spacing of (100) plane recovers to the original value at the re-charged state of 3 V (Fig. 2e), indicating the reversible (de) intercalation processes confirmed by operando XRD as well.

Based on the above results, the pseudo-rectangular current response and pseudo-linear voltage response were realized based on the Na^+ (de) intercalations. Thus, the electrochemical kinetics analysis was used to investigate the relation of measured current (i) and sweep rate (v). A series of CV for Na^+ storage were measured at various rates from 0.2 to 10 mV s^{-1} (Figs. 2f and S6a). The CV shape is pseudo-rectangular, indicating capacitive behavior. CV curves for Li^+ intercalation storage at various sweep rates from 0.2 to 1 mV s^{-1} also show a similar capacitive behavior (Fig. S6b). The relation of measured current (i) and sweep rate (v) can be presented by the following Equation (1):

$$i = av^b \tag{1}$$

Where the b is the slope of log (i) *vs.* log (v) plots at a specific potential. A b-value of 0.5 indicates diffusion-controlled process, whereas b-value of 1 indicates surface-controlled process. Figs. 2g and S6c show the change of b-value about Na^+ and Li^+ storage, respectively. For Na^+ storage, all of b-value are very close to 1 rather than 0.5, which suggests the domination of pseudocapacitive charge storage process. Especially, the b-value for Na^+ storage is higher than that for Li^+ storage, indicating highly capacitive Na^+ storage property.

The total current responds (i) can be divided into two parts: capacitive responds (k_1v) and diffusion-controlled responds ($k_2v^{1/2}$), which can be presented by the following Equation (2):

$$i(\mathrm{V}) = k_1v + k_2v^{1/2} \tag{2}$$

The quantitative analysis is firstly calculated at the sweep rate of 1 mV s^{-1}. The capacitive contribution of CV curve is 93% and 83% for Na^+ and Li^+ storage, respectively (Fig. 2h and Fig. S6d). As shown in Fig. S6e, the value of capacitive contribution enhances with the increase of the sweep rate. These results confirm that the sodium-ion intercalation process of $FeVO_4{\cdot}0.6H_2O$ in 1–3 V *vs.* Na^+/Na exhibit exceptional pseudocapacitive features. The detailed charge storage mechanism of $FeVO_4{\cdot}0.6H_2O$ for Na^+ storage in 1–3 V *vs.* Na^+/Na is schematically shown in Fig. 2i. Different from the traditional battery-type intercalation anode, $FeVO_4{\cdot}0.6H_2O$ presents reversible Na^+ intercalation pseudocapacitance behavior.

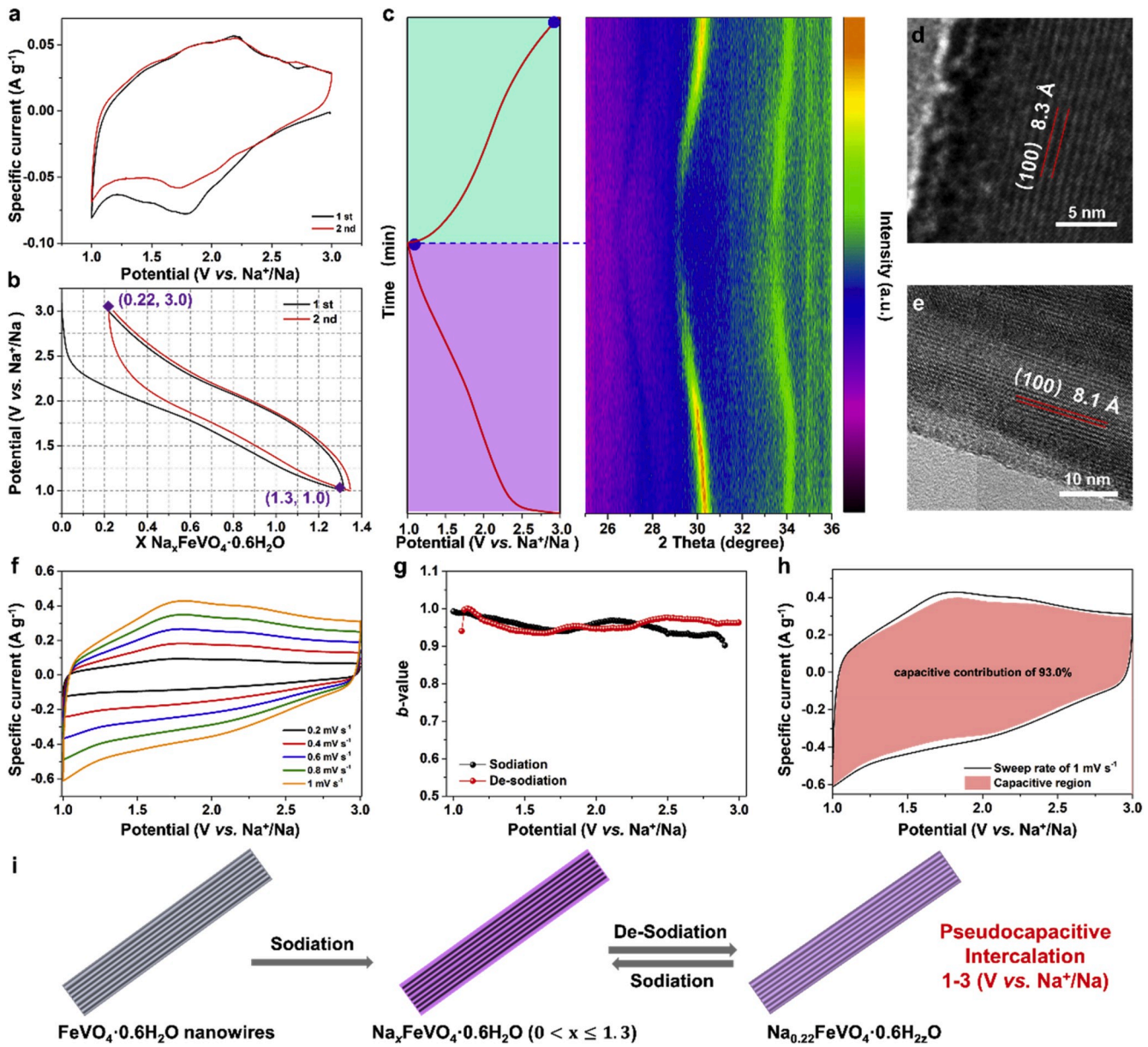

Fig. 2. Pseudocapacitive sodium-ion intercalation behavior of $FeVO_4$ 0.6H_2O nanowires. For Na^+ storage in 1–3 V *vs.* Na^+/Na, CV curves (a) and potential *vs.* composition profiles (b) of $FeVO_4$·0.6H_2O nanowires, respectively. (c) Operando XRD pattern during galvanostatic test at 0.1 A g^{-1}. (d, e) *Ex-situ* HRTEM images of $FeVO_4$·0.6H_2O nanowires when discharged to 1 V *vs.* Na^+/Na and charged to 3 V *vs.* Na^+/Na, respectively. (f) CV curves of $FeVO_4$·0.6H_2O nanowires in 1–3 V *vs.* Na^+/Na at different sweep rates from 0.2 to 1 mV s^{-1}. (g) Analysis of *b*-value at different potential. (h) Separation of the capacitive and diffusion contribution at a sweep rate of 1 mV s^{-1}. (i) A schematic diagram of pseudocapacitive Na^+ intercalation mechanism for $FeVO_4$·0.6H_2O nanowires.

3.4. Rate capability and long-term cycling stability of Na^+ intercalation reaction

The electrochemical performance for Li^+ and Na^+ storage is compared and analyzed based on intercalation reaction. The rate capacity of $FeVO_4$·0.6H_2O anode from 0.1 to 10 A g^{-1} is shown in Fig. 3a. At the current density of 0.1 A g^{-1}, the sodiation capacity is 169 mAh g^{-1}, which is similar to the lithiation capacity (158 mAh g^{-1}). At a higher current density of 6 A g^{-1}, the sodiation capacity is 60 mAh g^{-1}, which is higher than lithiation capacity of 21 mAh g^{-1}. At 10 A g^{-1}, the sodiation capacity remains 40 mAh g^{-1}. A better rate performance of $FeVO_4$·0.6H_2O for Na^+ storage is probably due to that a larger Na^+ presents a lower activation energy of ionic diffusion and smaller Stokes' radius in solvent, resulting in higher mobility of $[Na\text{-solvent}]^+$ and ionic conductivity than those of Li^+ [20,21]. The related GV curves at different currents present a typical capacitive-like shape (Fig. 3b).

The cycling performance was tested at the current density of 2 A g^{-1} (Fig. 3c). The sodiation capacity is 86 mAh g^{-1} after 2000 cycles, corresponding to a capacity retention of 83% (calculated based on the capacity at second cycle), which is higher than the result of Li^+ storage (40 mAh g^{-1} after 2000 cycles with a capacity retention of 36%). Interestingly, the $FeVO_4$·0.6H_2O exhibits better cycling performance for Na^+ storage. This comparison indicates that the (de)intercalation of Na^+ is much reversible that those of Li^+, although the former leads to lager volume expansion but the lattice is highly recoverable (Fig. 2c). The related charge-discharge curves at different cycles are presented in Fig. S7a, all of which show the linear slops in 1–3 V *vs.* Na^+/Na. Especially, the lithiation and sodiation capacity show an increasing trend in the first 70 cycles and then gradually decrease during (de)intercalation process. For explaining the phenomena, the *ex-situ* XRD patterns in 1–3

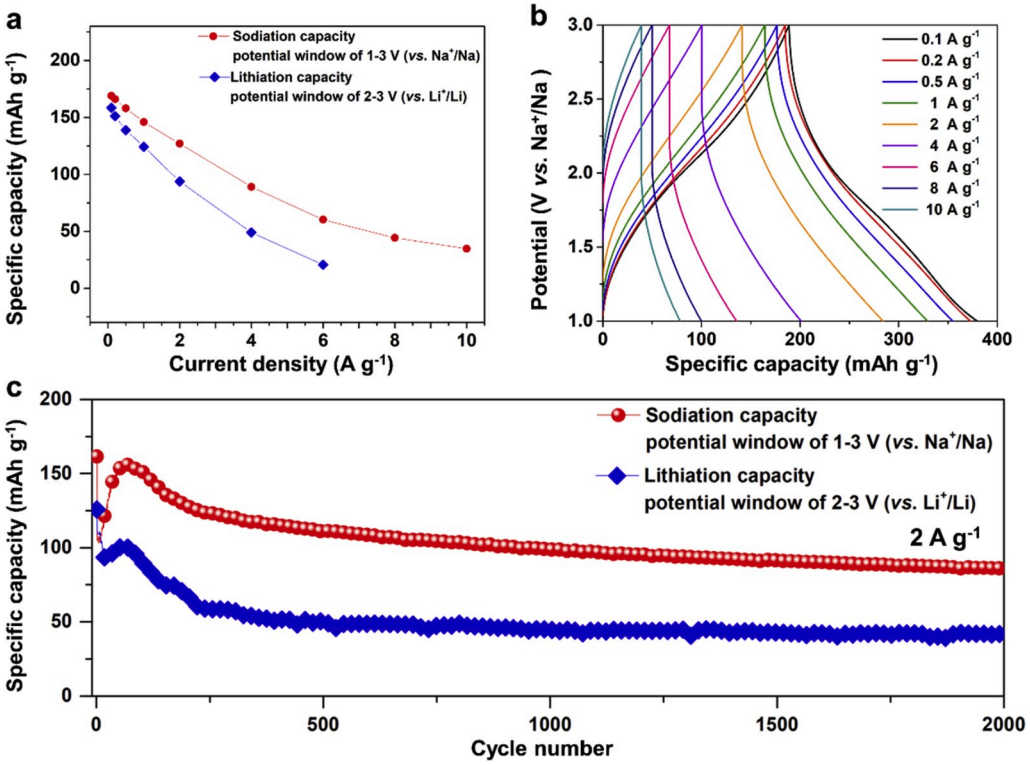

Fig. 3. The electrochemical performance of $FeVO_4{\cdot}0.6H_2O$ nanowires with pseudocapacitive intercalation reaction for Li^+ and Na^+ storage. Rate performance (a) and long-term cycling performance at 2 A g^{-1} (c) of the $FeVO_4{\cdot}0.6H_2O$ nanowires for Li^+ and Na^+ storage. (b) The related GV curves for Na^+ storage at different rate.

V *vs.* Na^+/Na are presented in Fig. S7b. All of the diffraction peaks of $FeVO_4{\cdot}0.6H_2O$ after 50 cycles still exist, but they partially widen or disappear after 1000 cycles, indicating that $FeVO_4{\cdot}0.6H_2O$ would have the trend of partly amorphous transformation after long-term cycles. The result shows that the increase of capacity during the initial cycles may be an activation process and the followed capacity decay is related to the slightly amorphous transformation. The realization of pseudocapacitive intercalation reaction greatly enhances the rate and cycling performance of Na^+ storage, which is very promising for developing high performance SICs.

3.5. *Hybrid sodium-ion capacitor based on pseudocapacitive intercalation $FeVO_4{\cdot}0.6H_2O$ anode*

To further demonstrate the potential of $FeVO_4{\cdot}0.6H_2O$ anode in SIC, a SIC was assembled by $Na_3(VO)_2(PO_4)_2F$/rGO (NVOPF/rGO) cathode and $FeVO_4{\cdot}0.6H_2O$ anode. The phase of the prepared NVOPF/rGO material is confirmed by XRD (Fig. S8a). The SEM image (Fig. S8b) displays nanorod morphology of NVOPF. Determined by the CHNS elemental analysis, the carbon content of NVOPF/rGO is 6.28 wt%. NVOPF/rGO is a Na-rich battery-type cathode with high-rate capability (Fig. S9) [42–44]. The NVOPF/rGO can provide the de-intercalated Na^+ into the $FeVO_4{\cdot}0.6H_2O$ anode which delivers high ICE and excellent pseudocapacitive performance. In this case, the very complex and unsafe pre-sodiation treatment on the anode side is avoided, which could largely reduce the manufacturing processes and cost. Based on the capacity balance, the weight ratio of cathode: anode is 2:1. The total capacity and energy density of SICs are based on both mass of positive and negative materials. At first, as schematically shown in Fig. 4a, the three-electrode device by using sodium as reference (which is not involved in the electrochemical reaction) is used to record the electrochemical operation potential of each anode and cathode, respectively. This method is very important and useful to deeply investigate the operation function and mechanism of a whole device. The GV charge-discharge curves of the three-electrode device (Fig. 4b) at 1 C (1 C is defined as the current density of a full-discharge for 1 h) show the typical capacitor-like triangular shapes. The voltage windows of both electrodes barely change after cycling for 40 h, indicating that the full cells show high reversibility. Fig. 4c shows the charge-discharge profiles and actual potential (*vs.* Na^+/Na) of cathode and anode at high rates. The charge or discharge potential of cathode and anode shifts with the increase of current density, owing to their different rate behavior and the internal resistance of the SIC. Thanks to the three-electrode device, it clearly proves that the potential shifts of cathode and anode are within the range of just 0.05 V. The actual operating potential of NVOPF/rGO cathode is within 3.5–4.1 V (*vs.* Na^+/Na), and $FeVO_4{\cdot}0.6H_2O$ anode safely works in 0.9–3.1 V (*vs.* Na^+/Na), indicating the excellent safety and stability of the SIC even at high rates. The assembled SIC makes full use of the two plateaus of the NVOPF/rGO cathode and the pseudocapacitive intercalation of $FeVO_4{\cdot}0.6H_2O$, maximizing energy density of the devices even without any pre-sodiation treatments.

The two-electrode cell was assembled to confirm actual application. The operation mechanism of SIC is shown in Fig. 5a. During charge process, the Na^+ ions de-intercalate from NVOPF/rGO cathode and then intercalate into the $FeVO_4{\cdot}0.6H_2O$ anode. At the discharge process, the Na^+ ions move on the contrary. The charge-discharge curves at 0.06 A g^{-1} (Fig. 5b) display a pseudo-linear voltage response. The ICE of the SIC is 83%, which mainly depends on the ICE of $FeVO_4{\cdot}0.6H_2O$ anode. The SIC is assembled without any pre-sodiation on the anode material, highlighting the significance of high ICE of anode materials. The electrochemical impedance spectra (EIS) of SIC (Fig. S10) shows small high-frequency semicircles, referred to the low charge transfer resistance (R_{ct}) of ~5 Ohm, indicating a fast charge transfer process. Subsequently, the rate performance of the SIC was tested based on two-electrode systems (Fig. 5c), which was basically consistent with the result of the three-electrode results. The SIC delivers a high discharge capacity of ~54

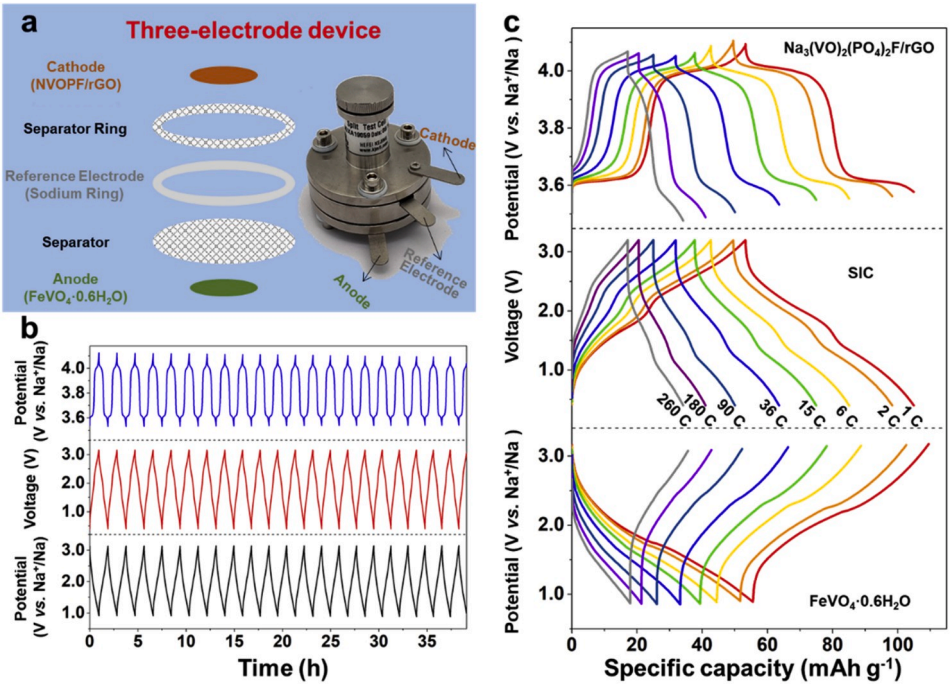

Fig. 4. Electrochemical performance of the SIC based on three-electrode systems. (a) The schematic of three-electrode device. (b) Cycle-life behavior of the cathode, anode and full cell in the SIC during charge-discharge cycling, respectively. (c) The charge-discharge curves of the cathode, anode and full cell at different current density, respectively.

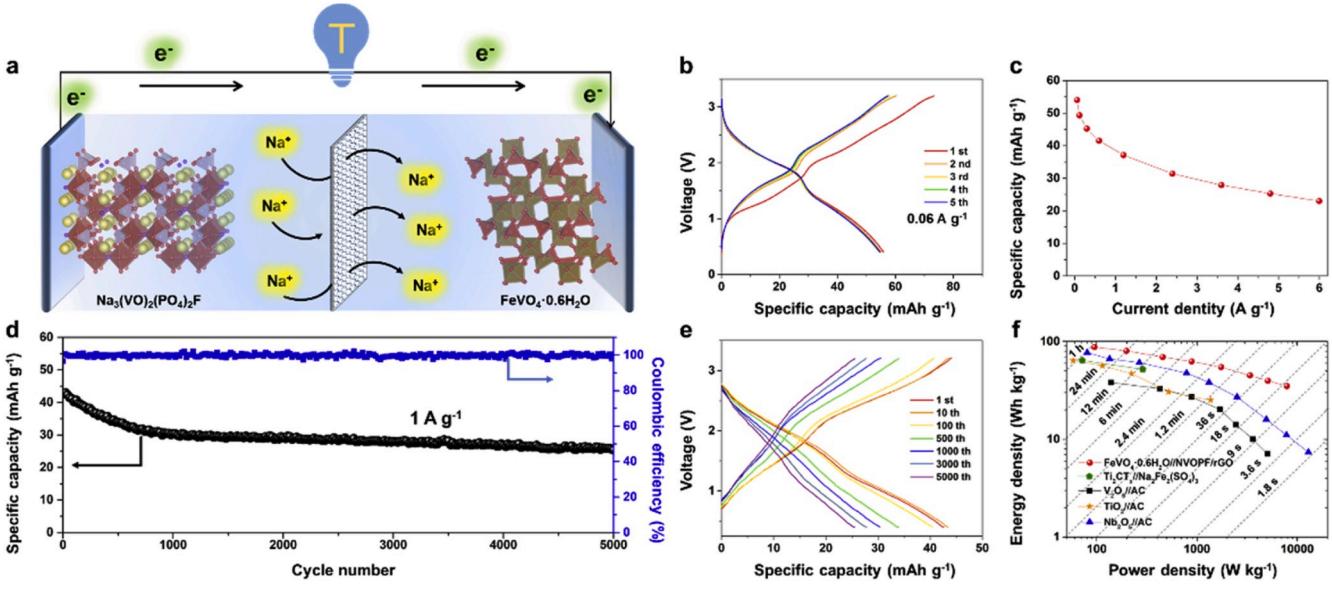

Fig. 5. Electrochemical performance of the SIC based on two-electrode systems. (a) Schematic diagram of $FeVO_4·0.6H_2O$//NVOPF/rGO SIC. The charge-discharge curves at 0.06 A g^{-1} (b) and the rate capacity (c) of the SIC. (d, e) Long-term cycling performance of the SIC and the related charge-discharge curves at different cycles at 1 A g^{-1}. (f) Ragone plots of $FeVO_4·0.6H_2O$//NVOPF/rGO SIC, and the comparisons with the reported state-of-the art SIC: V_2O_5//AC [45], TiO_2//AC [46], Nb_2O_5//AC [28], Ti_2CT_x//$Na_2Fe_2(SO_4)_3$ [47].

mAh g^{-1} at 0.06 A g^{-1} (1 C). The SIC displays excellent high-rate performance: a reversible capacity of ~42 mAh g^{-1} at 0.6 A g^{-1} (15 C), 31 mAh g^{-1} at 2.4 A g^{-1} (90 C) and 25 mAh g^{-1} at 4.8 A g^{-1} (260 C). Long-term stability of the SIC at the high rate of 1 A g^{-1} (24 C) is shown in Fig. 5d, after initial cyling at low current density (Fig. S11). The capacity retention maintains at 70%, 65%, 60% after 1000, 2000 and 5000 cycles. The related charge-discharge curves of the SIC (Fig. 5e) remain similar during the long-term cycles.

Energy density and average power density of the SIC were calculated based on the results of rate performance, as shown in the Ragone plots (Fig. 5f). The SIC exhibits a maximum energy density of 88 Wh kg^{-1} at a power density of 95 W kg^{-1}. At the high power of 0.9, 1.7 and 3.4 kW kg^{-1}, the delivered energy density is 63, 55, 45 Wh kg^{-1}, respectively. When the output power ability is much enlarged to 7.9 kW kg^{-1}, the energy density is 35 Wh kg^{-1}. Comparing to the reported state-of-the-art SICs, even those anodes had additional electrochemical presodiation treatment [28,45–47], our assembled SIC delivers much better high energy and power density, as well as ultra-long cycling stability.

4. Conclusion

In conclusion, pseudocapacitive sodium-ion intercalation of $FeVO_4{\cdot}0.6H_2O$ nanowires is demonstrated and successfully applied in the assembly of a novel SIC. The deep sodiation (or lithiation) reaction of $FeVO_4{\cdot}0.6H_2O$ anode is separated into two steps: ion intercalation and amorphization transformation. Especially, it is proved that Na^+ intercalation reaction of $FeVO_4{\cdot}0.6H_2O$ presents a pseudocapacitive behavior. The pseudocapacitive sodium-ion storage behavior (93% of capacity from the pseudocapacitance at a sweep rate of 1 mV s^{-1}) naturally enables the high-rate ability. In addition, the pseudocapacitive sodium-ion intercalation of $FeVO_4{\cdot}0.6H_2O$ anode delivers high capacity, high ICE, remarkable rate capability and cycling stability. We have demonstrated the $FeVO_4{\cdot}0.6H_2O$ as an effective anode for developing a new prototype of SIC. In this case, previous complex and unsafe pre-sodiation processes are waived. Based on the intuitive evaluation of three-electrode system, the electrode in $FeVO_4{\cdot}0.6H_2O$//NVOPF/rGO SIC shows a tiny potential drift (0.05 V), which is conductive to realize the long-term cycles and high safety of SIC. The $FeVO_4{\cdot}0.6H_2O$//NVOPF/rGO SIC delivers a high specific energy of 88 Wh kg^{-1} (with a power density of 95 W kg^{-1}) and power density of 7.9 kW kg^{-1} (with an energy density of 35 Wh kg^{-1}), as well as stable 5000 cycles. This work presents the significant advantages of intercalation pseudocapacitance for obtaining both high energy and high power SICs.

Declaration of competing interest

The authors declare that they have no known competing financial interests or personal relationships that could have appeared to influence the work reported in this paper.

CRediT authorship contribution statement

Jun Dong: Conceptualization, Investigation, Writing - original draft, Visualization. **Yi He:** Conceptualization, Investigation, Writing - original draft, Visualization. **Yalong Jiang:** Formal analysis, Validation, Writing - review & editing. **Shuangshuang Tan:** Formal analysis, Validation, Writing - review & editing. **Qiulong Wei:** Supervision, Data curation, Conceptualization, Writing - review & editing, Funding acquisition. **Fangyu Xiong:** Writing - review & editing. **Zhaolong Chu:** Writing - review & editing. **Qinyou An:** Formal analysis, Validation, Writing - review & editing. **Liqiang Mai:** Supervision, Data curation, Conceptualization, Writing - review & editing, Funding acquisition.

Acknowledgements

This work was supported by the National Natural Science Foundation of China (51832004, 51521001), the National Key Research and Development Program of China (2016YFA0202603), the Program of Introducing Talents of Discipline to Universities (B17034), the Yellow Crane Talent (Science & Technology) Program of Wuhan City, Foshan Xianhu Laboratory of the Advanced Energy Science and Technology Guangdong Laboratory (XHT2020-003), the XMU Undergraduate Innovation and Entrepreneurship Training Programs (202010384009).

Appendix A. Supplementary data

Supplementary data to this article can be found online at https://doi.org/10.1016/j.nanoen.2020.104838.

References

[1] P.K. Nayak, L. Yang, W. Brehm, P. Adelhelm, Angew. Chem. Int. Ed. 57 (2018) 102–120.
[2] J. Ding, W. Hu, E. Paek, D. Mitlin, Chem. Rev. 118 (2018) 6457–6498.
[3] R. Thangavel, K. Kaliyappan, K. Kang, X. Sun, Y.S. Lee, Adv. Energy Mater. 6 (2016) 1502199.
[4] H. Wang, C. Zhu, D. Chao, Q. Yan, H.J. Fan, Adv. Mater. 29 (2017) 1702093.
[5] C. Vaalma, D. Buchholz, M. Weil, S. Passerini, Nat. Rev. Mater. 3 (2018) 1–11.
[6] C. Grey, J. Tarascon, Nat. Mater. 16 (2017) 45–56.
[7] C. Cui, H. Wang, M. Wang, X. Ou, Z. Wei, J. Ma, Y. Tang, Small 15 (2019) 1902659.
[8] G. Zhang, X. Ou, C. Cui, J. Ma, J. Yang, Y. Tang, Adv. Funct. Mater. 29 (2019) 1806722.
[9] D. Mazouzi, B. Hammouti, J. Mater. Environ. Sci. 12 (2019) 1194–1199.
[10] M.S. Whittingham, J. Electrochem. Soc. 123 (1976) 315.
[11] M.S. Whittingham, F.R. Gamble Jr., Mater. Res. Bull. 10 (1975) 363–371.
[12] M. Whittingham, Belgian Patent No. 819672, 1975.
[13] M.S. Whittingham, Science 192 (1976) 1126–1127.
[14] M.S. Whittingham, Prog. Solid State Chem. 12 (1978) 41–99.
[15] Y. Liu, H. Wang, L. Cheng, N. Han, F. Zhao, P. Li, C. Jin, Y. Li, Nano Energy 20 (2016) 168–175.
[16] J.B. Cook, H.S. Kim, T.C. Lin, C.H. Lai, B. Dunn, S.H. Tolbert, Adv. Energy Mater. 7 (2017) 1601283.
[17] F. Sauvage, L. Laffont, J.-M Tarascon, E. Baudrin, Inorg. Chem. 46 (2007) 3289–3294.
[18] Z. Jian, W. Han, X. Lu, H. Yang, Y.-S. Hu, J. Zhou, Z. Zhou, J. Li, W. Chen, D. Chen, L. Chen, Adv. Energy Mater. 3 (2013) 156–160.
[19] Q. Wei, J. Liu, W. Feng, J. Sheng, X. Tian, L. He, Q. An, L. Mai, J. Mater. Chem. 3 (2015) 8070–8075.
[20] K. Kubota, M. Dahbi, T. Hosaka, S. Kumakura, S. Komaba, Chem. Rec. 18 (2018) 459–479.
[21] Q. Liu, H. Wang, C. Jiang, Y. Tang, Energy Storage Mater 23 (2019) 566–586.
[22] J. Chen, D.H. Chua, P.S. Lee, Small Methods 4 (2020) 1900648.
[23] H. Wang, C. Zhu, D. Chao, Q. Yan, H.J. Fan, Adv. Mater. 29 (2017) 1702093.
[24] V. Augustyn, P. Simon, B. Dunn, Energy Environ. Sci. 7 (2014) 1597–1614.
[25] J.W. Kim, V. Augustyn, B. Dunn, Adv. Energy Mater. 2 (2012) 141–148.
[26] M. Zukalová, M. Kalbác, L. Kavan, I. Exnar, M. Graetzel, Chem. Mater. 17 (2005) 1248–1255.
[27] T. Brezesinski, J. Wang, S.H. Tolbert, B. Dunn, Nat. Mater. 9 (2010) 146–151.
[28] E. Lim, C. Jo, M.S. Kim, M.H. Kim, J. Chun, H. Kim, J. Park, K.C. Roh, K. Kang, S. Yoon, Adv. Funct. Mater. 26 (2016) 3711–3719.
[29] K. Lan, Q. Wei, R. Wang, Y. Xia, S. Tan, Y. Wang, A. Elzatahry, P. Feng, L. Mai, D. Zhao, J. Am. Chem. Soc. 141 (2019) 16755–16762.
[30] X. Xu, F. Xiong, J. Meng, X. Wang, C. Niu, Q. An, L. Mai, Adv. Funct. Mater. (2020) 1904398.
[31] S. Denis, E. Baudrin, M. Touboul, J.M. Tarascon, J. Electrochem. Soc. 144 (1997) 4099.
[32] P. Poizot, E. Baudrin, S. Laruelle, L. Dupont, M. Touboul, J.-M. Tarascon, Solid State Ionics 138 (2000) 31–40.
[33] H. Zhang, K. Ye, K. Zhu, R. Cang, J. Yan, K. Cheng, G. Wang, D. Cao, Electrochem. Acta 256 (2017) 357–364.
[34] Z. Fang, F. Fan, Z. Ding, C. Wang, L. Long, S. Hao, Mater. Res. Bull. 48 (2013) 1737–1740.
[35] X. Liu, Y. Cao, H. Zheng, C. Feng, Mater. Lett. 187 (2017) 15–19.
[36] Y.V. Kaneti, Z. Zhang, J. Yue, X. Jiang, A. Yu, J. Nano Res. 15 (2013) 1948.
[37] Q. An, F. Lv, Q. Liu, C. Han, K. Zhao, J. Sheng, Q. Wei, M. Yan, L. Mai, Nano Lett. 14 (2014) 6250–6256.
[38] W.S. Hummers Jr., R.E. Offeman, J. Am. Chem. Soc. 80 (1958), 1339-1339.
[39] S. Denis, R. Dedryvere, E. Baudrin, S. Laruelle, M. Touboul, J. Olivier-Fourcade, J. Jumas, J. Tarascon, Chem. Mater. 12 (2000) 3733–3739.
[40] M.R. Palacin, Chem. Soc. Rev. 38 (2009) 2565–2575.
[41] S. Fang, D. Bresser, S. Passerini, Adv. Energy Mater. 10 (2020) 1902485.
[42] Z. Zhang, Z. Chen, Z. Mai, K. Peng, Q. Deng, A. Bayaguud, P. Zhao, Y. Fu, Y. Yu, C. Zhu, Small 15 (2019), e1900356.
[43] D. Chao, C.H. Lai, P. Liang, Q. Wei, Y.S. Wang, C. Zhu, G. Deng, V.V. Doan-Nguyen, J. Lin, L. Mai, Adv. Energy Mater. 8 (2018) 1800058.
[44] Y. Yin, F. Xiong, C. Pei, Y. Xu, Q. An, S. Tan, Z. Zhuang, J. Sheng, Q. Li, L. Mai, Nano Energy 41 (2017) 452–459.
[45] Z. Chen, V. Augustyn, X. Jia, Q. Xiao, B. Dunn, Y. Lu, ACS Nano 6 (2012) 4319–4327.
[46] Z. Le, F. Liu, P. Nie, X. Li, X. Liu, Z. Bian, G. Chen, H.B. Wu, Y. Lu, ACS Nano 11 (2017) 2952–2960.
[47] X. Wang, S. Kajiyama, H. Iinuma, E. Hosono, S. Oro, I. Moriguchi, M. Okubo, A. Yamada, Nat. Commun. 6 (2015) 1–6.